ACCSCIENCE PUBLISHING

International Journal of Bioprinting

RESEARCH ARTICLE

Hollow spherical mineralized scaffold integrated with a bone marrow mesenchymal stem cell-laden three-dimensional delivery system for regeneration of critical-sized bone defects

Xiao Liu[1,2†], Zhengyang Chang[1,2,3†], Zijian Li[1,2,3†], Jianpeng Gao[1,2], Hufei Wang[1,2], Jie Wu[1,2], Jiazhi Yan[1,2,3], Jianheng Liu[1,2], Licheng Zhang[1,2*], Daohong Liu[1,2*], Wei Zhang[1,2*], and Ming Li[1,2*]

[1]Department of Orthopaedics, The Fourth Medical Center of the Chinese PLA General Hospital, Beijing, China

[2]Department of Orthopaedics, National Clinical Research Center for Orthopedics, Sports Medicine & Rehabilitation, Beijing, China

[3]Department of Orthopaedics, Medical School of Chinese PLA, Beijing, China

[†]*These authors contributed equally to this work.*

***Corresponding authors:**
Ming Li
(liming891215@163.com)
Wei Zhang
(bszw@hotmail.com)
Daohong Liu
(domb@vip.sina.com)
Licheng Zhang
(zhanglcheng218@126.com)

Citation: Liu X, Chang Z, Li Z, *et al*. Hollow spherical mineralized scaffold integrated with a bone marrow mesenchymal stem cell-laden three-dimensional delivery system for regeneration of critical-sized bone defects. *Int J Bioprint*. 2026:12(2):026050046.
doi: 10.36922/IJB026050046

Received: February 1, 2026

Revised: March 15, 2026

Accepted: March 20, 2026

Published online: April 23, 2026

Abstract

Treating critical-sized bone defects is a significant clinical challenge. Three-dimensional (3D) printing combined with bone tissue engineering (BTE) has emerged as a promising strategy for bone regeneration; however, key limitations persist, including a mismatch between scaffold degradation and osteogenesis, as well as insufficient bioactivity. In this study, we aimed to fabricate a hollow spherical mineralized biphasic calcium phosphate scaffold by 3D printing (photopolymerization via digital light processing) and incorporated within its cavity a 3D delivery system composed of methacryloyl-modified gelatin hydrogel loaded with bone marrow mesenchymal stem cells (BMSCs). The composite scaffold was systematically evaluated using material characterization, *in vitro* cytocompatibility analysis, and *in vivo* rabbit bone defect models. Our findings demonstrated that the scaffold exhibited favorable mechanical properties, biocompatibility, and enhanced osteogenic differentiation, migration, and pro-osteogenic gene expression in BMSCs. Notably, the scaffold effectively repaired critical-sized bone defects in rabbit models within 12 weeks. This novel BTE composite scaffold provides a groundbreaking design philosophy and an innovative therapeutic strategy for complex bone defect repair.

Keywords: 3D printing; Biphasic calcium phosphate; Mineralized modification; Spherical hollow structure; 3D culture; Bone regeneration

1. Introduction

Bone defects arising from trauma, infection, tumor resection, or congenital abnormalities pose a significant clinical challenge worldwide.[1] Bone defects are highly prevalent, with traumatic injuries contributing to millions of cases annually.[2] The treatment of bone defects is complex and is frequently complicated by nonunion, delayed union, or failure of healing, resulting in persistent disability and deformity.[3] In some cases, traditional

treatment methods, such as autografts and allografts, are effective. However, they are limited by donor site morbidity, limited availability, and immune rejection risk.[4,5] Consequently, there is a pressing need for innovative approaches to overcome these limitations and provide reliable long-term solutions for bone-defect repair.

In recent years, bone tissue engineering (BTE) has emerged as a promising new strategy that can overcome the limitations of conventional treatments by combining biomaterials, cells, and bioactive factors to regenerate functional bone tissue. This approach addresses the critical issues of availability and biocompatibility and opens new avenues for personalized and minimally invasive therapies. However, BTE scaffold materials are not permanent replacements for defective bones. During bone reconstruction, the scaffold inevitably undergoes degradation. Therefore, even if the scaffold closely mimics the morphology of natural bone before implantation, it gradually loses its predefined structure *in vivo*.[6] Residual irregular scaffold architecture often impedes new bone ingrowth and the reconstruction of interconnected bone tissue because of insufficient vascularization,[7,8] inadequate degradation,[9,10] fibrous encapsulation,[11] and mismatch between material degradation and new bone formation.[12] Accordingly, we proposed a new concept of scaffold modification—osteogenesis requiring a temporary bone shelter, also referred to as the empty shell osteogenesis concept.[13] Based on this concept, we previously designed hollow spherical structured scaffolds.[14] The hollow-structure design was used to release the internal space that accommodated the rate of new bone formation, creating an optimal space for the ingrowth of new bone tissue and forming a highly interconnected vascular network. The spherical configuration of the scaffolds allowed for mutual point contact in the three-dimensional (3D) structure, enabling sufficient interaction between the tissue fluid and scaffold while preserving the extracellular matrix (ECM) environment. This structural design has shown promising results in the repair of critical-sized bone defects.

A critical challenge in BTE lies in effective stem cell delivery, which serves as a pivotal determinant of material bioactivity.[15,16] Traditional two-dimensional (2D) cell seeding strategies significantly deviate from *in vivo* physiological conditions, characterized by restricted spatial cell growth, frequent induction of contact inhibition, and potential alteration of native phenotypic characteristics.[17,18] In contrast, 3D delivery systems permit cellular expansion in a 3D orientation, maintain the natural morphology while enhancing ECM secretion, strengthen intercellular adhesion and communication, and more faithfully recapitulate the native tissue microenvironment. This approach effectively preserves the biochemical and structural components of cellular niches, demonstrating superior cellular biological properties compared to 2D delivery systems.[19,20] Among the most promising seed cells for bone repair, bone marrow mesenchymal stem cells (BMSCs) can secrete osteogenic ECM components within the defect microenvironment, promote autonomous osteogenic differentiation, and enhance calcium deposition, thereby accelerating osseous regeneration.[21,22] Achieving effective delivery in 3D culture systems requires meticulous carrier selection.

Methacryloyl-modified gelatin (GelMA), a photo-crosslinkable protein hydrogel derived from ECM components, shares homologous amino acid sequences with collagen, an intrinsic organic constituent of bone tissue.[23] GelMA forms stable hydrogel networks through ultraviolet (UV)-initiated crosslinking in the presence of photoinitiators. Its porous 3D architecture exhibits high permeability to oxygen, nutrients, and hydrophilic metabolites,[24] while providing an ECM-mimetic microenvironment characterized by an optimal structural topography for cellular proliferation/differentiation, exceptional biocompatibility, cell-instructive properties, and tunable biodegradability.[25] GelMA is widely adopted for 3D cell culture, tissue engineering, and bioprinting applications due to the abovementioned attributes.[26] However, 3D delivery solely relying on hydrogel-encapsulated osteogenic key seed cells fails to construct an osteoconductive substitution platform at bone-defect sites and lacks sufficient mechanical support capacity for the damaged region.[27] This technological limitation necessitates hybrid systems that integrate GelMA with BTE scaffolds to create multifunctional composites. Such combinatorial strategies enhance mechanical resilience and endow scaffolds with cell-instructive capabilities, enabling the activation of osteogenic transcriptional cascades and amplifying the intrinsic bone regenerative potential.[28]

This study builds on our previous research,[13,14] employing 3D printing technology to fabricate structurally optimized biphasic calcium phosphate (BCP) spherical hollow scaffolds with surface modifications through *in situ* mineralization technology to enhance the osteoinductive capacity.[29] Furthermore, using the GelMA hydrogel as a 3D culture carrier for BMSCs—key stem cells in osteogenic microenvironments—we constructed an intracavitary GelMA hydrogel-based BMSCs delivery system within the hollow architecture of the scaffolds. This integrated design provides biomimetic BMSCs growth niches and amplifies the osseous regenerative potential, thereby providing a novel strategic framework for BTE applications in bone-defect repair.

2. Materials and methods

2.1. Preparation of 3D-printed micropore mineralized scaffolds

The 3D configuration of the micropore mineralized scaffolds (MiPM) was engineered using Materialize Magics 19.0 (Materialize, Belgium) to generate Standard Tessellation Language-formatted digital models. Key geometrical specifications include a 4 mm external diameter, 0.5 mm wall thickness, and uniform 300 μm pore channels.

Biphasic calcium phosphate constructs were manufactured using digital light processing (DLP) additive technology. The photopolymerizable system consisted of diphenyl (2,4,6-trimethylbenzoyl) phosphine oxide (1.17 g/cm^3; Sinopharm Chemical Reagent Co., Ltd., China) as a photoinitiator and Solsperse 17000 (Qian'an Chemical Co., Ltd., China) as a dispersant. Ceramic feedstock containing nano-hydroxyapatite (nano-HA)/β-tricalcium phosphate (β-TCP) (ratio: 15/85, d50 = 2 μm) was homogenized with B-0# photosensitive resin (type B-0#, Ten Dimensions Technology Co., Ltd., China) incorporating the aforementioned additives. A planetary ball-milling system (Qiagen, United States of America [USA]) facilitated a 3-h dispersion processing to achieve slurry homogeneity.

The aforementioned slurry was introduced into the trough of the DLP printer (AUTOCERA-L, Ten Dimensions Technology Co. Ltd., China), with the following printing parameters: an exposure power density of 24.5 mW/cm^2, an exposure time of 5 s for each layer, and a slice layer thickness of 25 μm. The fabricated scaffolds were subjected to thermal treatment in a high-temperature furnace, undergoing sintering at 1,200 °C for 3 h to completely remove the photosensitive resin components.

The simulated body fluid was prepared according to the protocol established by Kokubo *et al.*[30], with the pH adjusted to 7.40 using Tris buffer solution (50 mmol/L tris(hydroxymethyl)aminomethane + 0.1 M hydrochloric acid). The scaffolds were immersed in the simulated body fluid at a mass-to-volume ratio of 1 g:40 mL in glass vessels and subjected to dynamic incubation on an orbital shaker (175 rpm, 48 h). Post-treatment specimens were sequentially rinsed with deionized water through vacuum filtration and dried at 110 °C through hydrothermal treatment before characterization.

2.2. Preparation of GelMA solution and dissolution solution

GelMA (5% w/v) was dissolved in phosphate-buffered saline (PBS; pH 7.4) containing 0.25% (w/v) lithium phenyl-2,4,6-trimethylbenzoylphosphinate as the photoinitiator. The mixture was sterilized using a 0.22 μm filter and stored at 4 °C protected from light.

The lyophilized GelMA dissolution powder (EFL Co., Ltd., China) was dissolved in 2 mL of sterile PBS under aseptic conditions. Following filtration through a 0.22 μm sterile membrane, a 50 mg/mL stock solution of the GelMA dissolution agent was obtained. The working solution was prepared by diluting the stock solution with a standard complete culture medium to a final concentration of 0.3 mg/mL.

2.3. Characterization analysis

2.3.1. Scanning electron microscopy

The MiPM scaffolds were mounted onto the specimen stub using a double-sided conductive adhesive tape. A gold sputter coating process was performed under a high vacuum (10^{-4} Pa) with a magnetron sputter coater (MC1000, Hitachi, Japan), during which the specimens were rotated at 10 rpm for uniform deposition. The operational parameters included an accelerating voltage of 10 kV and a coating duration of 60 s. After coating, the scaffolds were loaded into the scanning electron microscopy (SEM) sample chamber for observation.

A 5% (w/v) GelMA solution was prepared and crosslinked under UV light to form a hydrogel. The cured hydrogel was immersed in liquid nitrogen for 10 min and lyophilized for 48 h. The freeze-dried GelMA scaffold was sectioned along the central axis to expose its cross-sectional surface. For SEM imaging, the sample was mounted on the detection stage using double-sided conductive tape and sputter-coated under the aforementioned parameters. Finally, the coated samples were transferred to the SEM chamber for observation and imaging.

2.3.2. X-ray diffraction

The MiPM scaffold was ground into a uniformly fine powder. Next, 50 mg of the powder was compressed into a translucent pellet. After pellet preparation, X-ray diffraction (XRD) analysis was performed using an X-ray diffractometer (D8 Advance, Bruker, Germany) under the following conditions: a tube current of 40 mA, a tube voltage of 40 kV, and a copper target wavelength of 1.5406 Å.

2.3.3. Fourier-transform infrared spectroscopy

The lyophilized GelMA flocculent solid was ground into a fine powder, and 5 mg of the powder was mixed with 500 mg of potassium bromide. The mixture was ground until the particle size was <2 μm. The mixed powder was compressed uniformly using a hydraulic press at 800 MPa to form a thin pellet. The Fourier-transform infrared

(FTIR) spectra of these sheets were recorded using an FTIR spectrometer (FTIR spectrometer, Nicolet 570, WI, USA) over the wavenumber range of 400–4,000 cm^{-1} at a resolution of 4 cm^{-1} using 32 scans.

2.3.4. Nuclear magnetic resonance

A 10 mg sample of GelMA flocculent solid was dissolved in deuterium oxide. After complete dissolution, the solution was transferred into a nuclear magnetic resonance (NMR) tube. Solution-state NMR analysis was performed using an AVANCE 600 spectrometer (Bruker, Germany) with the following parameters: a rotor diameter of 3.2 mm and a spinning speed of 10 kHz.

2.3.5. Mechanical properties test

The mechanical properties of the scaffolds were assessed using an electronic universal testing machine (Norwood, MA, USA) at room temperature. The disk height was set at 4 mm. The compression test was conducted at a crosshead speed of 0.5 mm/min, and each group of scaffolds was subjected to five measurements.

2.3.6. Degradation test

The initial weight (*W0*) of MiPM was recorded, after which scaffolds were incubated in PBS at 37 °C with the solution refreshed every two days. At designated time points (days 5, 10, 15, 20, 25, 30, 35, 40, 45, 50, 55, 60, 65, 70, 75, and 80), samples were retrieved, rinsed with deionized water, blotted dry, and weighed to obtain *Wt*. The remaining weight was calculated as:

$$\text{Remaining weight}(\%) = (\text{Wt} / \text{W0}) \times 100\% \quad (1)$$

2.4. *In vitro* cytology testing

The Orthopedic Laboratory of the PLA General Hospital provided the BMSCs used in this experiment. Cell generation was expanded up to the third generation using α-MEM medium supplemented with fetal bovine serum (10%) and penicillin–streptomycin (1%). The cells were maintained in a controlled environment at 37 °C with 5%CO_2 and the medium was replaced every other day.

2.4.1. Extract preparation

Scaffold extracts were prepared according to the International Organization for Standardization (ISO 10993-12:2009) protocol.[31] After preparation, the scaffold was immersed in a culture medium at 37 °C for 48 h. The mixture was centrifuged at 1,500 rpm for 10 min, followed by filtration through a 0.22 μm membrane to collect the supernatant. The scaffold extract was prepared as a 100% concentration solution at a ratio of 6 cm^2/mL, which was subsequently diluted to 50% for experimental use.

2.4.2. Cell Counting Kit-8

Bone marrow mesenchymal stem cells were cultured in extracts of different scaffolds for 1, 3, and 5 days. After incubation with Cell Counting Kit-8 (CCK-8; 10%; Dojindo, CK18, Japan) reagent for 1 h, cell viability was evaluated by measuring the optical density at 450 nm using a microplate reader (Thermo MK3, Thermo Fisher, USA). Each experiment was performed in triplicate.

2.4.3. Live/Dead staining

For the co-culture of cells and materials, BMSCs were prepared as a single-cell suspension at a density of 1×10^4 cells/mL and seeded into a 12-well plate (800 μL per well). After the cells had adhered to the plate, the culture medium was replaced with extract solutions from different materials, and the cultures were incubated for 24 and 72 h. For cell seeding on the scaffold surface, sterile scaffolds were pre-wetted by immersing them in α-MEM medium in a 24-well plate for 15 min. After removing the scaffolds, a 1 mL cell suspension containing 1.5×10^4 cells was carefully added. The BMSCs were then seeded onto the scaffolds and cultured in the medium for 120 h. Following incubation, Live/Dead viability dye was applied for 15 min, and cell viability was visualized under a confocal microscope (LSM880, ZEISS, Germany), where green and red fluorescence indicated live and dead cells, respectively. The ImageJ software (https://imagej.net/ij/) was used for cell detection. Each experiment was performed in triplicate.

2.4.4. Phalloidin staining

Bone marrow mesenchymal stem cells were cultured for 24 h according to the method described in Section 2.4.2. Subsequently, the cells were immersed in 4% (w/v) paraformaldehyde solution for 30 min to fix the cells and washed thrice with PBS. The cells were stained with phalloidin for 30 min. The morphology of the cytoskeleton on the scaffold surface was observed using a confocal microscope (LSM880, ZEISS, Germany).

2.4.5. Migration experiment using Transwell assay

Bone marrow mesenchymal stem cells were seeded in the upper chamber (8 μm pore size) of a Transwell insert (8-μm pore size, Corning, NY, USA) placed in a 24-well plate at a density of 1×10^4 cells/well. Then, the cells were cultured in low-serum medium (α-MEM supplemented with 2% fetal bovine serum and 1% penicillin–streptomycin) for 6 h. After fixation, the non-migrated cells on the upper chamber membrane were removed using a cotton swab. The migrated cells were stained with 1% crystal violet for 5 min. After staining, the cells were observed under a light microscope (Nikon, Tokyo, Japan) , and ImageJ was used

for cell detection.

2.4.6. Scratch wound assay

Bone marrow mesenchymal stem cells (2×10^5 cells/well) were seeded in 6-well plates and cultured with complete medium (α-MEM containing 10% fetal bovine serum and 1% penicillin-streptomycin) until reaching 80–90% confluency. After washing twice with PBS, a straight scratch wound was created in the cell monolayer using a sterile 1000 μL pipette tip. The dislodged cells were removed by washing, and the remaining cells were incubated for 12 h in low-serum MiPM extracts, MiPM/Gel extracts, MiPM/Gel/BMSCs extracts, and medium (α-MEM supplemented with 1% fetal bovine serum and 1% penicillin–streptomycin). The scratch healing degree was subsequently measured using the ImageJ software.

2.4.7. Quantitative real-time polymerase chain reaction

Bone marrow mesenchymal stem cells were seeded at a density of 10×10^4 cells/well in 6-well plates and cultured in a normal medium for 24 h. Subsequently, the medium was replaced with an osteogenic induction medium (50 μg/mL) ascorbic acid (Solarbio, Beijing, China), 10 mM β-glycerophosphate (Solarbio, Beijing, China), 100 nM dexamethasone (Solarbio, Beijing, China). After 7 days of culture, total RNA was extracted from the cells using Trizol reagent (G3013; Servicebio, China), followed by quantitative real-time polymerase chain reaction (RT-qPCR) analysis. Each sample was analyzed in triplicate.

2.4.8. Alkaline phosphatase staining and activity analysis

Bone marrow mesenchymal stem cells were seeded in 24-well plates at a density of 2×10^4 cells/well. After cell adhesion, the α-MEM medium was replaced with osteogenic induction extract (50 mM ascorbic acid, 10 mM β-glycerophosphate, 100 nM dexamethasone). On days 7 and 14, the cells were fixed with 1 mL of 4% paraformaldehyde for 30 min. Subsequently, 1 mL of alkaline phosphatase (ALP) staining solution (Beyotime, China) was added, and the cells were stained at 37 °C under light-protected conditions for 30 min and washed thrice with PBS. ALP staining was observed under an inverted stereomicroscope (SMZ25, Nikon, Japan). The supernatant was analyzed using an ALP detection kit (P0321S, Beyotime, China) and a Bicinchoninic Acid kit (P0012, Beyotime, China) to measure ALP activity and total protein content, respectively. ALP activity was normalized to the total intracellular protein concentration. Each experiment was performed in triplicate.

2.4.9. Alizarin Red S staining and quantification

Bone marrow mesenchymal stem cell seeding, osteogenic induction extract preparation, and osteogenic induction processes were performed according to the method described in Section 2.4.8. On days 14 and 21, the cells were fixed with 1 mL of 4% paraformaldehyde for 30 min, followed by staining with 1 mL of Alizarin Red S (ARS) staining solution (Solarbio, China) at 37 °C for 10 min. After three washes with PBS, the stained cells were observed under an inverted stereomicroscope (SMZ25, Nikon, Japan). Finally, 10% cetylpyridinium chloride was added to solubilize the stained calcium deposits for quantitative analysis. Each experiment was performed in triplicate.

2.5. *In vivo* biological testing

2.5.1. Modeling of critical-sized bone defects

We randomly divided 48 male New Zealand white rabbits (aged 24 weeks and body weight: 3.1 ± 0.9 kg) into 4 groups (blank, MiPM, MiPM/Gel, and MiPM/Gel/BMSCs; $n = 12$ per group). At each time point (4, 8, and 12 weeks), four rabbits from each group were euthanized for analysis. Briefly after inducing anesthesia, the left distal femur was shaved and disinfected. A skin incision was made, followed by blunt dissection of the muscle to expose the femoral condyle. A cylindrical defect (8 mm in diameter) was created in the distal femur using a surgical drill to preserve the integrity of the contralateral cortex. Sterile scaffolds were implanted into the defect sites according to group allocation, and the subcutaneous tissue and skin were sutured in layers. The animals were euthanized at 4, 8, and 12 weeks postoperatively for subsequent analyses.

2.5.2. Micro-computed tomography analysis

New bone formation in rabbits across different experimental groups was assessed by micro-computed tomography (CT) using the Inveon MM system (Siemens, Germany). The scanning parameters were set as follows: voltage 80 kV, current 500 μA, effective pixel size 17.34 μm, and exposure time 1500 ms. The region of interest was defined as a cylindrical area with a diameter of 8 mm and a depth extending to the contralateral cortex. Following the scan, the Inveon Research Workplace software (Siemens, Germany) was employed for 3D image reconstruction and analysis of osteogenesis-related parameters, including bone mineral density (BMD), bone volume/total volume (BV/TV), trabecular thickness (Tb.Th), and trabecular spacing (Tb.Sp).

2.5.3. Histology analysis

After fixation with 4% paraformaldehyde, the specimens were dehydrated through a graded ethanol series (70% → 80% → 90% → 95% → 100%), cleared with xylene, and embedded in paraffin. The embedded blocks were sectioned into 10-μm slices using a microtome. The sections were subjected to hematoxylin and eosin (H & E) and Masson's trichrome staining to evaluate the histological and collagen deposition patterns, respectively. The selected regions were examined under a light microscope, and representative images were captured for analysis.

2.6. Statistical Analysis

Statistical analyses were performed using GraphPad Prism 8 software (Version 10.1.0, GraphPad Software, USA). Normality was verified using the Shapiro–Wilk test. Continuous variables are expressed as mean ± standard error. For comparisons between the two groups, an independent Student's *t*-test and the Mann–Whitney *U* test were applied for normally and non-normally distributed data, respectively. Multi-group comparisons were performed using a one-way analysis of variance with Tukey's post-hoc test. All experiments were performed in triplicate, unless otherwise specified. Statistical significance was defined as $^{*}p < 0.05$, $^{**}p < 0.01$, $^{***}p < 0.001$, $^{****}p < 0.0001$.

3. Results

3.1. Characterization Analysis

The MiPM scaffold, fabricated using the DLP printing technology and integrated with an intracavitary GelMA hydrogel-based 3D BMSC culture system, demonstrated a composite structural morphology (Figure 1A). SEM analysis at 100× magnification revealed a lamellar stacking architecture on the scaffold surface (Figure 1(Bi)), a characteristic feature consistent with the bottom-up layer-by-layer printing mechanism inherent in DLP additive manufacturing. Under high magnification (10,000×), heterogeneous mineralized nodules with diameters ranging from 0.1 to 1.0 μm were observed adhering to the micropore surfaces (Figure 1(Bii)), confirming successful biomimetic mineralization modification on the scaffold surface. Lyophilized GelMA exhibited a highly porous and interconnected microstructure (Figure 1(Biii)), providing an optimal 3D structural framework for cellular proliferation and differentiation. XRD

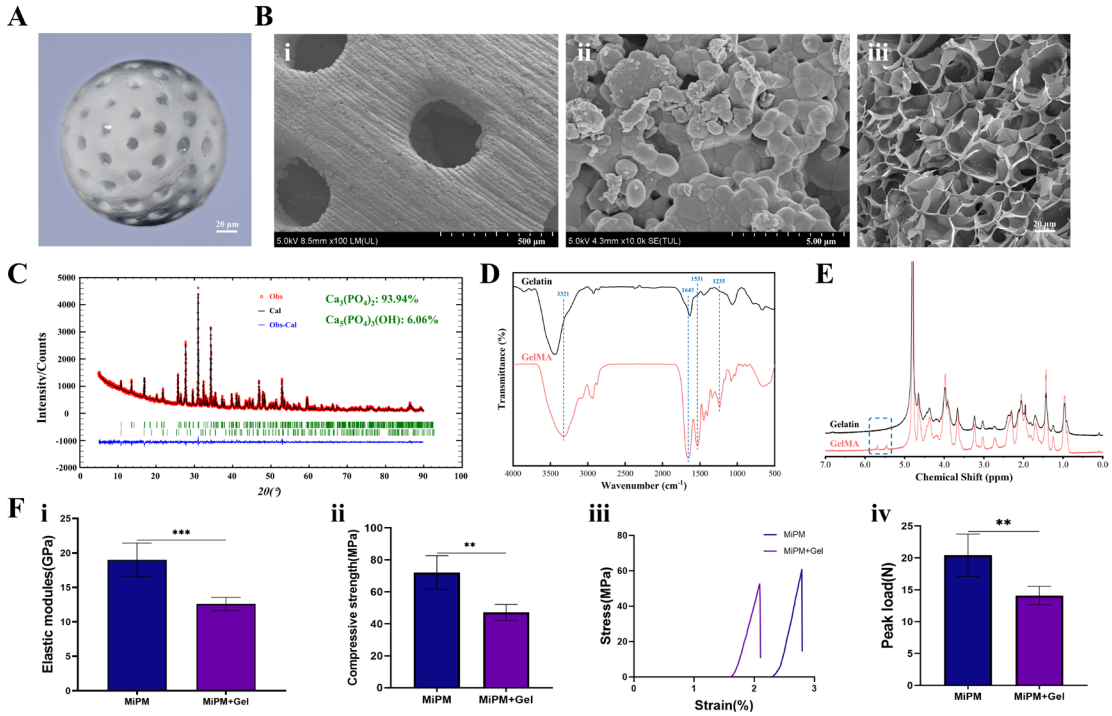

Figure 1. Characterization analysis. (A) Overall morphology of digital light processing-printed composite structural scaffold. Scale bars: 20 μm; magnification: 1.0×. (B) Scanning electron microscopy results for micropore mineralized scaffold (MiPM) and methacryloyl-modified gelatin (GelMA). i. Scale bars: 500 μm; magnification: 100×. ii. Scale bars: 5 μm; magnification: 10,000×. iii. Scale bars: 20 μm; magnification: 400×. (C) X-ray diffraction results of the MiPM. (D) Fourier transform infrared spectroscopy test results for gelatin and GelMA. (E) Nuclear magnetic resonance test results for gelatin and GelMA. (F) Results of the mechanical properties test performed on MiPM and MiPM/GelMA. i. elastic moduli, ii. compressive strength, iii. stress–strain curves, iv. peak load. The quantitative results were expressed as mean ± standard error of the mean ($n = 5$); significance levels were indicated as $^{*}p < 0.05$, $^{**}p < 0.01$, $^{***}p < 0.001$.

analysis confirmed the phase composition of mineralized MiPM scaffolds as 93.94% β-TCP and 6.06% HA (Figure 1C). Fourier-transform infrared spectroscopy (FTIR) spectroscopy of GelMA revealed characteristic absorption bands: a sharp peak at 1,230 cm^{-1} corresponding to C–N stretching vibrations of amide groups induced by gelatin methacryloylation. The spectral region of 1,500–1,570 cm^{-1} was attributed to C–N–H bending modes, while the broadband spanning 3,200–3,400 cm^{-1} indicated the presence of peptide bonds and hydroxyl (–OH) functionalities. A distinct peak at 1,643 cm^{-1} demonstrated C=C stretching vibrations from methacrylate groups, confirming successful double bond conjugation (Figure 1D). High-resolution ^{1}H NMR spectroscopy revealed the characteristic proton resonances at 5.5 and 5.7 ppm (Figure 1E), confirming successful grafting of methacryloyl groups onto gelatin side chains through covalent conjugation. Mechanical characterization demonstrated elastic moduli of 18.99 ± 2.45 GPa for pristine MiPM scaffolds and 12.58 ± 0.97 GPa for composite scaffolds, respectively, both falling within the range of human cortical bone (7–30 GPa).[2] Structural failure occurred in the MiPM scaffolds at strains <2.5%, indicating higher brittleness compared to the composite system (Figure 1F). Additionally, during an 80-day *in vitro* degradation observation, the MiPM scaffolds demonstrated a sustained degradation trend but were not completely degraded (Figure S1).

3.2. *In vitro* cytology testing

Proliferation evaluation results via CCK-8 assay demonstrated that the cell proliferation activity increased in a time-dependent manner in all four groups during the culture period. No significant differences were observed among the groups on day 1, but with prolonged culture time, the MiPM/Gel/BMSCs composite system exhibited the strongest cell proliferation capacity, showing significant differences compared with other groups by day 5 ($p < 0.0001$). These findings indicate that the composite scaffold system possesses excellent biocompatibility and superior proliferation-promoting effects (Figure 2A). To verify the biocompatibility of the materials, we further employed Live/Dead staining. Because the pre-loaded cells in the MiPM/Gel/BMSCs group would interfere with the accuracy of material property assessment, we utilized the MiPM and MiPM/Gel groups to evaluate the direct effects of the scaffold materials and their coatings on cell viability. After co-culturing the two groups with BMSCs for 24 and 72 hours, the viable cell counts increased substantially with prolonged culture time and minimal apoptosis, indicating robust proliferative activity (Figure 2B,C). After 24 h of culture, the average viable cell counts per field were 67.33 ± 24.01 (MiPM) and 101.33 ± 8.39 (MiPM/Gel), and nonviable cell counts were 2.67 ± 1.53 (MiPM) and 4.33 ± 2.31 (MiPM/Gel) (Figure 2(Bi)). At 72 h, these values increased to 159.00 ± 14.11 (MiPM) versus 262.33 ± 13.32 (MiPM/Gel) for viable cells and 5.33 ± 3.06 (MiPM) versus 7.33 ± 3.51 (MiPM/Gel) for nonviable cells (Figure 2(Bii)), reaching statistical significance ($p < 0.05$). These results demonstrated that the gel-coated scaffold maintained excellent biocompatibility comparable to the bare scaffold while further promoting BMSC proliferation. Following a 5-day culture of BMSCs on the material surfaces, Live/Dead staining revealed effective cell adhesion to both MiPM and MiPM/Gel scaffolds, with uniform distribution, preserved morphology, and negligible dead cell attachment (Figure 2C). Phalloidin staining revealed that BMSCs cultured on MiPM scaffolds exhibited intact morphology with intercellular connectivity, demonstrating spindle-shaped configurations and enhanced cellular extension upon partial confluence. In comparison, the MiPM/Gel group demonstrated enhanced cellular extension capacity and sustained elongated spindle morphology (Figure 2D).

According to the Transwell assay results (Figure 3A), MiPM scaffolds (93.33 ± 4.16) enhanced cell transmigration compared with the blank group (64.67 ± 2.52), supporting a migration-promoting effect of the scaffold material. The MiPM/Gel group (125.00 ± 4.08) exhibited further enhancement in transmigrated cell numbers, indicating that gelatin coating augmented the cell migration-promoting capacity of the scaffold.[32-34] Notably, MiPM/Gel/BMSCs composites exhibited the strongest migration activity, with the highest migrated cell numbers (174.33 ± 9.71) and densest distribution, confirming a significantly enhanced biological activity for the material after BMSC loading (Figure 3B). In the scratch wound assay (Figure 3C), the blank group showed the lowest wound healing level after a 12-h culture, reflecting a limited inherent cell migration capacity. The MiPM scaffold group demonstrated significantly enhanced wound healing compared with the blank group, confirming the migration-promoting effects of the scaffold material; the MiPM/Gel group showed an even greater improvement compared with MiPM alone, indicating that gelatin coating augmented cell migration capacity. The MiPM/Gel/BMSCs group displayed superior wound healing ability compared with the other groups; this was consistent with Transwell assay findings, strongly indicating that the BMSC-loaded composite material was the most effective in promoting cell migration (Figure 3D).

Bone marrow mesenchymal stem cells were co-cultured with different material groups and subjected to osteogenic induction for 7 days. RT-qPCR was performed to detect the expression of osteogenesis-related genes (*COL1A1*, *BGLAP*, and *SPP1*) in BMSCs to evaluate the impact of the

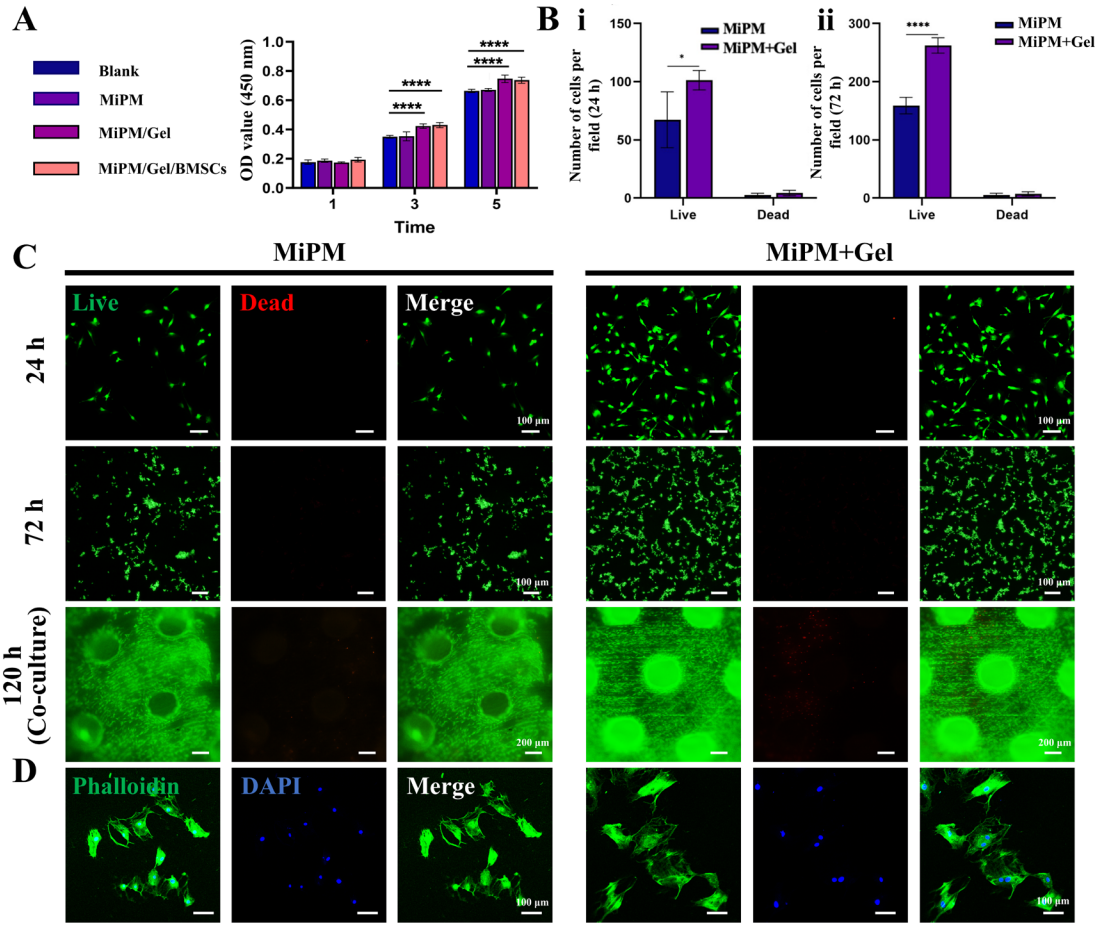

Figure 2. *In vitro* cytology testing. (A) Cell viability of bone marrow mesenchymal stem cells (BMSCs) evaluated via the CCK-8 test on days 1, 3, and 5 post–co-culture with diverse materials ($n = 3$). (B) Quantitative analysis of viable and dead cell counts in co-cultures with MiPM and MiPM/Gel (i. 24 h, ii. 72 h). (C) Live/Dead staining of BMSCs co-cultured with extracts from MiPM and MiPM/Gel at 24 and 72 h, and BMSCs seeded on MiPM and MiPM/Gel scaffolds after 120 h of culture. Green represents living cells and red represents dead cells. (D) Phalloidin staining of BMSCs cultured with MiPM and MiPM/Gel for 24 h. Scale bars: 100 μm, 200 μm; magnification: 10×, 4×. The quantitative results were expressed as mean ± standard error of the mean ($n = 3$); significance levels were indicated as * $p < 0.05$, ** $p < 0.01$, *** $p < 0.001$, **** $p < 0.0001$.

materials on the osteogenic differentiation potential of the cells. mRNA levels of these osteogenesis-related genes were significantly elevated in all material groups compared with the blank control group, confirming effective induction of osteogenic gene expression by different materials (Figure 3E). Notably, the MiPM/Gel/BMSCs group exhibited the highest osteogenic gene expression levels, indicating its superior bone formation-promoting capacity.

As revealed through ALP staining, BMSCs exhibited a time-dependent enhancement in enzymatic activity, demonstrating a progressively deepening staining intensity with an extended osteogenic induction time (Figure 4A). Quantitative analysis revealed that the MiPM/Gel/BMSCs group showed significantly higher ALP activity levels at the corresponding time points ($p < 0.05$; Figure 4B). The quantitative data were consistent with the staining results, indicating that the MiPM/Gel/BMSCs group more effectively promoted ALP expression. ARS staining results demonstrated that the number of red mineralized calcium nodules progressively increased with prolonged osteogenic induction time (Figure 4C). Notably, BMSCs cultured in the MiPM/Gel/BMSCs group exhibited significantly higher mineralized nodule counts than the other control groups at all time points. Quantitative analysis further confirmed that all material groups effectively promoted calcium mineralization, with the MiPM/Gel/BMSCs group demonstrating the most superior mineralization capacity ($p < 0.05$; Figure 4D).

3.3. *In vivo* biological testing

The micro-CT results (Figure 5A) revealed that the bone defect area in the blank group remained visible at 4, 8, and 12 weeks. At 12 weeks, only minimal new bone

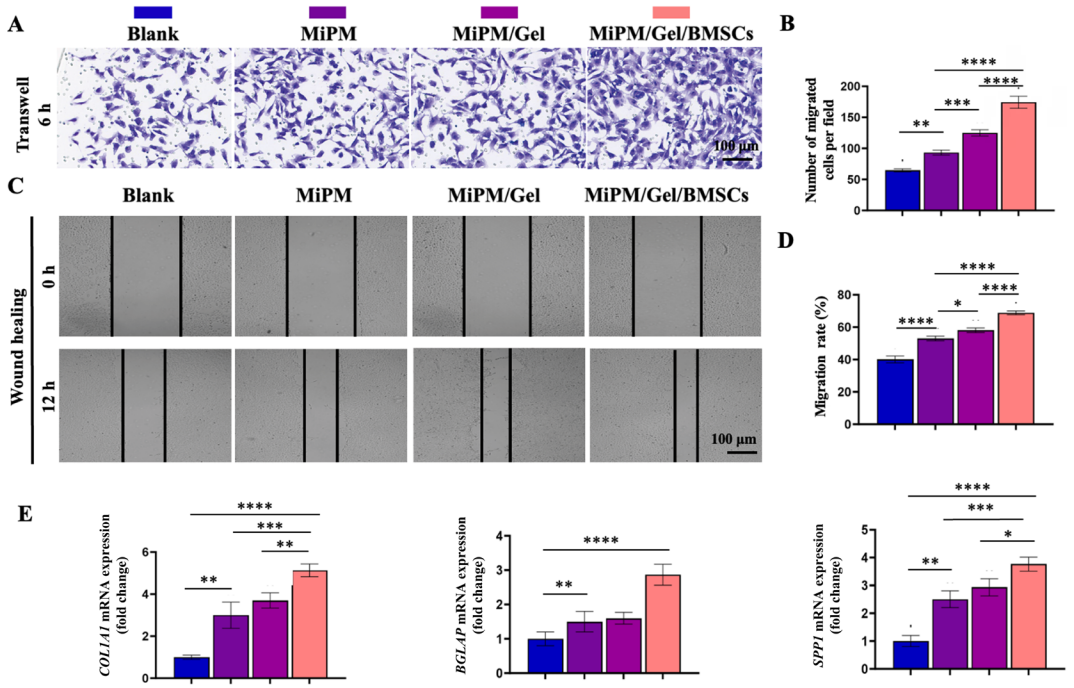

Figure 3. *In vitro* cytology testing. (A) Representative light microscopy images show the Transwell assay results at 6 hours. Scale bars: 100 μm; magnification: 10×. (B) Quantitative analysis of migrated cell numbers. (C) Representative light microscopy images show the scratch wound assay results at 0 and 12 h. Scale bars: 100 μm; magnification: 4×. (D) Quantitative analysis of wound healing rate. (E) The expression levels of osteogenic-related genes (*COL1A1*, *BGLAP*, and *SPP1*) were detected by RT-qPCR on day 7 of the experiment. The quantitative results were expressed as mean ± standard error of the mean ($n = 3$); significance levels were indicated as * $p < 0.05$, ** $p < 0.01$, *** $p < 0.001$, **** $p < 0.0001$.

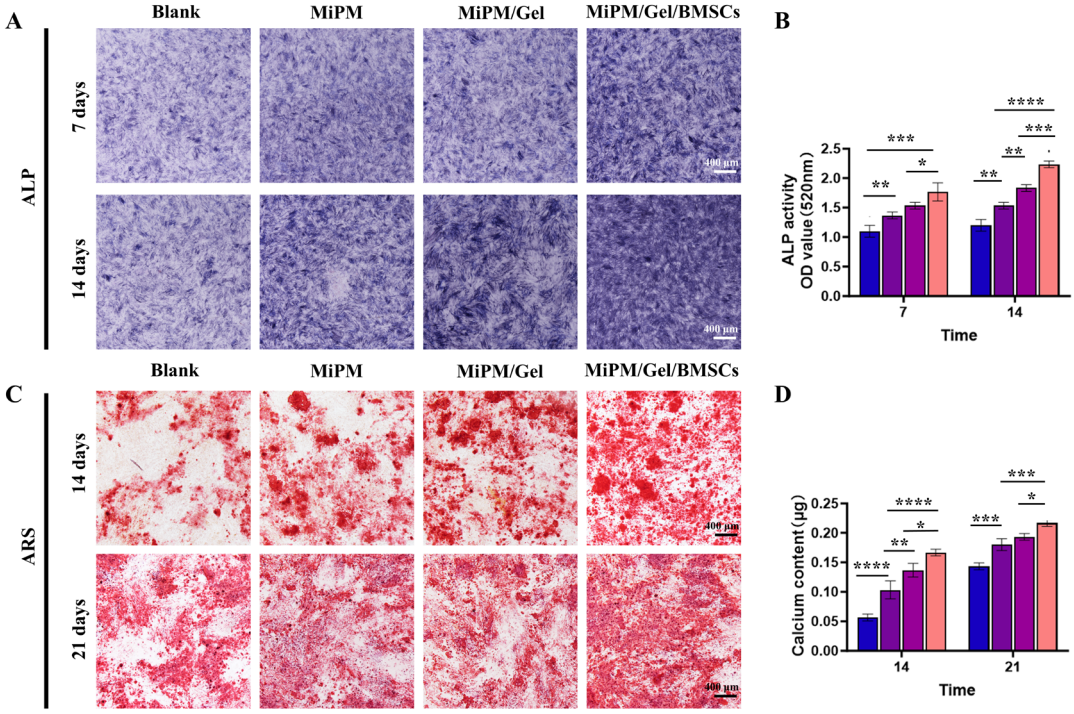

Figure 4. *In vitro* cytology testing: (A) Representative stereomicroscope images show alkaline phosphatase (ALP) staining at 7 and 14 days. (B) Quantitative analysis of ALP activity. (C) Representative stereomicroscope images show Alizarin Red S staining at 14 and 21 days. (D) Quantitative analysis of calcium content. The quantitative results were expressed as mean ± standard error of the mean ($n = 3$); significance levels were indicated as * $p < 0.05$, ** $p < 0.01$, *** $p < 0.001$, **** $p < 0.0001$.

formation was observed around the periphery of the defect, further validating that the 8-mm-diameter critical-sized bone defect constructed in this study could not heal spontaneously. In the MiPM group, new bone formation was observed on the scaffold surface at 4 weeks, with nascent bone infiltrating the scaffold interior through the surface pores. The bone volume within the hollow regions of the scaffold significantly increased at 8 weeks. At 12 weeks, external creeping bone growth covered the scaffold surface, and partial internal bone ingrowth was also evident. For the MiPM/Gel group, a grid-like pattern of new bone was formed on the scaffold surface within the defect area at 4 weeks; however, minimal bone ingrowth into the scaffold interior was observed. By weeks 8 and 12, some internal bone ingrowth within the scaffold was connected to the newly formed bone in the external defect region. The MiPM/Gel/BMSC group exhibited extensive new bone formation along the scaffold surface at 4 weeks, and the defect area was reduced significantly compared to other groups. Substantial bone ingrowth was observed within the scaffold, spanning its longest internal diameter. This phenomenon is likely attributable to the ability of the scaffold to deliver BMSCs effectively and support osteogenesis. At 8 weeks, this regenerative trend intensified; the defect area became nearly indistinguishable, and the newly formed bone exhibited a morphology consistent with the native bone tissue. The scaffold interior was densely filled with fresh bone tissue. At 12 weeks, a grid-like bone reconstruction matching the native bone structure was achieved in the defect area, and the scaffold interior was almost entirely occupied by new bone. These results demonstrate that the composite scaffold enabled efficient delivery of key seed cells for BTE, achieving robust repair of critical-sized bone defects.

The micro-CT 3D reconstruction results (Figure 5B) revealed that at 4 weeks, the blank group exhibited minimal new bone formation around the defect periphery in the sagittal view. In contrast, the coronal view showed a large central bone defect with insufficient bridging by new peripheral bone. In contrast, the MiPM and MiPM/Gel groups demonstrated partial creeping bone growth along the scaffold surface, utilizing the scaffold as an osteogenic platform. In addition, some bone ingrowth was observed within the scaffold interior; however, the regions with irregular bone defects persisted in both groups. The MiPM/Gel/BMSC group exhibited significantly more uniformly distributed new bone formation on the surface than the other groups, with the smallest residual bone defect area and substantial new bone formation observed on the scaffold surface and interior. At 8 weeks, the blank group displayed a prominent bone defect with minimal peripheral new bone formation, and the coronal view revealed a persistent, unrepaired through-and-through defect. In contrast, all three scaffold groups showed increased new bone volume compared to that at 4 weeks. Consistent with the micro-CT observations, the sagittal view demonstrated new bone enveloping the spherical scaffold surface, with grid-like new bone reconstruction around the scaffold, indicating effective bone creeping substitution using the scaffold as an osteogenic platform. At 12 weeks, the blank group exhibited slightly increased peripheral new bone formation compared to 8 weeks, but minimal new bone formation was observed within the defect core. The MiPM and MiPM/Gel groups showed almost complete scaffold surface coverage by new bone, with new bone filling scaffold gaps and forming interconnected grid-like structures within the defect. Remarkably, the MiPM/Gel/BMSC group achieved a uniform and morphologically mature new bone inside and outside the scaffold, fully replacing the critical-sized bone defect region.

Quantitative analysis of osteogenesis-related parameters from the micro-CT 3D reconstruction images (Figure 5C) revealed that the three scaffold groups exhibited significantly higher BMD, BV/TV, and Tb.Th, along with significantly lower Tb.Sp, compared to the blank group ($p < 0.05$). These results indicate that the scaffold groups formed thicker trabeculae and reduced intertrabecular spacing, demonstrating that the MiPM scaffold(developed based on our prior research)[14] and its composite derivatives (MiPM/Gel/BMSCs) effectively promoted new bone formation and trabecular ingrowth. Notably, the BV/TV values for the MiPM, MiPM/Gel, and MiPM/Gel/BMSCs groups were 71.45 ± 5.99%, 60.09 ± 7.99%, and 85.54 ± 5.31%, respectively, all exceeding 60%, indicating robust bone regeneration at the defect site. No statistically significant differences ($p > 0.05$) were observed in the osteogenic parameters (BMD, BV/TV, Tb.Th, and Tb.Sp) between the MiPM and MiPM/Gel groups. This suggests that constructing composite scaffolds by filling the MiPM scaffold with GelMA hydrogel did not impede bone ingrowth into the scaffold interior. In contrast, the MiPM/Gel/BMSC group exhibited significantly higher BMD, BV/TV, and Tb.Th, along with significantly lower Tb.Sp compared to the MiPM and MiPM/Gel groups ($p < 0.05$). These results demonstrated that the composite scaffold system, constructed based on the BCP hollow spherical structure to enable 3D BMSCs delivery, achieved superior bone regeneration efficacy at 12 weeks.

Hematoxylin and eosin staining results demonstrated that the blank group exhibited minimal new bone formation around the defect periphery, with virtually no bone ingrowth at the defect center. This observation aligns with the micro-CT findings, confirming that critical-

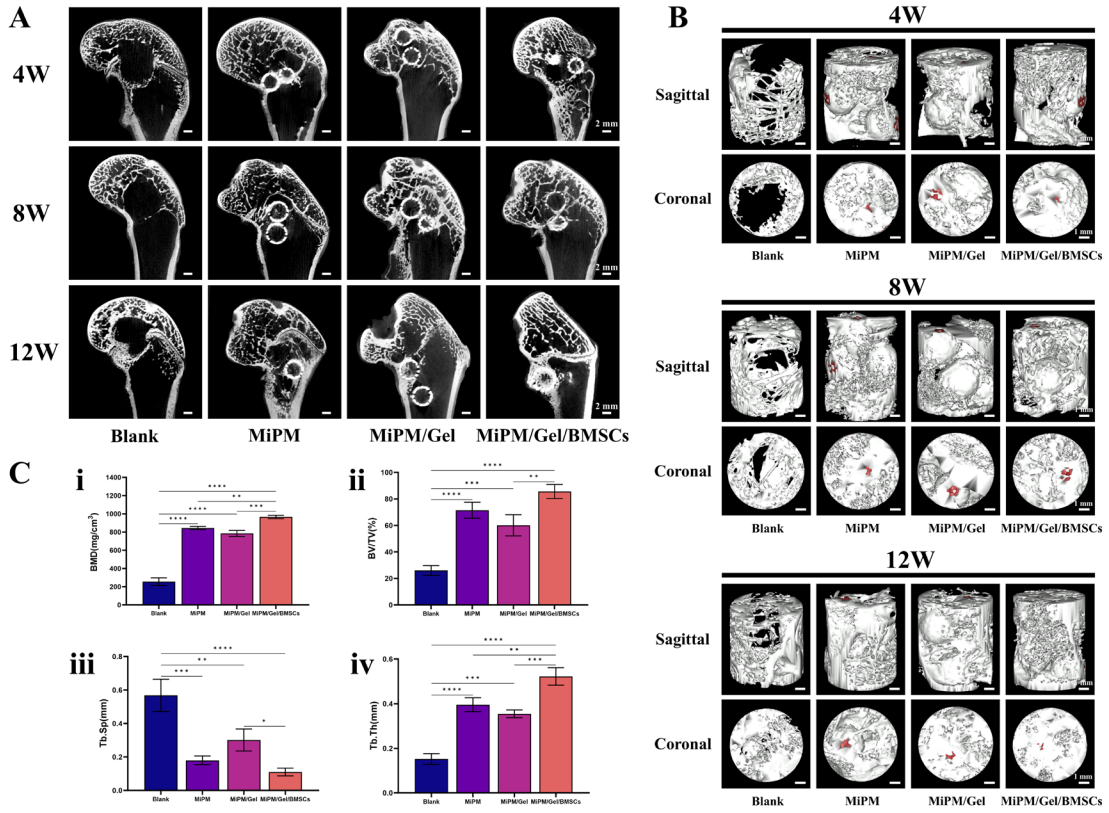

Figure 5. *In vivo* biological testing. (A) Micro-computed tomography (CT) of rabbit femoral condylar defects at 4, 8, and 12 weeks. (B) Micro-CT 3D reconstruction image of femoral condylar defects at 4, 8, and 12 weeks. (C) The microarchitectural parameters of newly formed bone. i. bone mineral density (BMD), ii. bone volume/total volume (BV/TV), iii. trabecular spacing (Tb.Sp), iv. trabecular thickness (Tb.Th). The quantitative results were expressed as mean ± standard error of the mean ($n = 4$); significance levels were indicated as * $p < 0.05$, ** $p < 0.01$, *** $p < 0.001$, **** $p < 0.0001$.

sized bone defects lack the inherent self-repair capability to bridge and guide regeneration without BTE scaffolds. In contrast, the MiPM and MiPM/Gel groups displayed new bone formation on the scaffold surfaces and within the interscaffold gaps, indicating the osteoconductive properties of the scaffolds in establishing an osteogenic platform. Notably, bone ingrowth was observed through the porous architecture of the scaffold in the hollow interior via interconnected pores. The MiPM/Gel/BMSCs group demonstrated an enhanced regenerative pattern. Extensive new bone not only migrated along scaffold surfaces but also formed uniformly distributed bone tissue within both the scaffold interior and external defect regions. This improvement was attributed to the effective delivery of the BMSCs, which synergized with the composite scaffold to amplify osteogenesis and matrix mineralization (Figure 6A). Masson staining results demonstrated a trend consistent with the H&E staining observations. At 12 weeks, all the scaffold groups remained partially undegraded. Notably, the MiPM/Gel/BMSC group exhibited significantly more newly formed trabecular bone on the scaffold surface and within its hollow interior (Figure 6B). *In vivo* biocompatibility was assessed by histological analysis of major organs. H & E staining of the heart, liver, spleen, lungs, and kidneys harvested at 12 weeks revealed no pathological changes in any of the scaffold groups. These results demonstrate the favorable biocompatibility of the implanted scaffolds (Figure S2). These findings indicate that the mineralized hollow spherical scaffold, which serves as an osteogenic platform, combined with the GelMA-based 3D BMSCs delivery system, synergistically enhanced trabecular bone ingrowth and creeping substitution, achieving superior repair of critical-sized bone defects.

4. Discussion

The compositional biomimicry, structural design, and bioactivity of BTE scaffolds are pivotal for critical-sized bone defect repair. In compositional replication, this study employed BCP—a composite of nHA and β-TCP—for 3D scaffold fabrication. XRD analysis confirmed the mineralogical congruence with natural bone matrix, inheriting spatial maintenance capacity and biocompatibility of nHA alongside the osteogenic

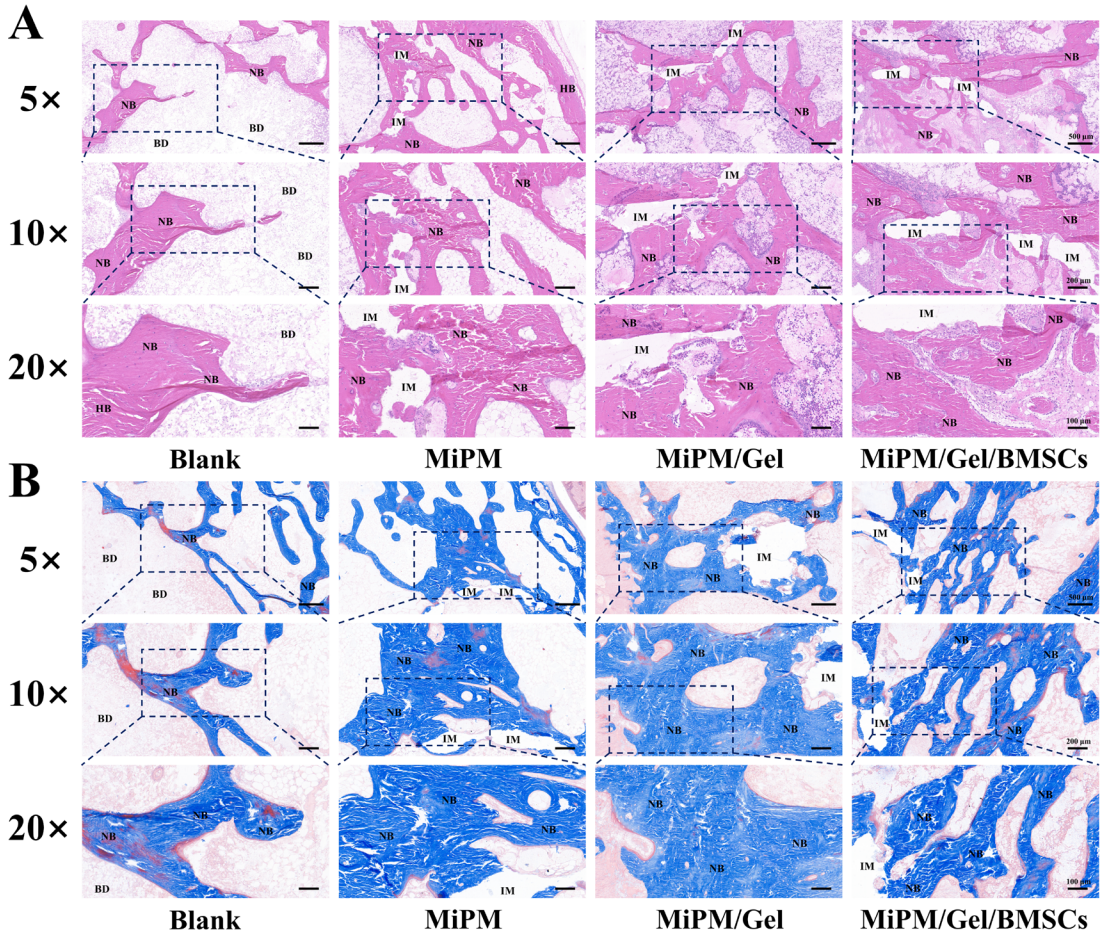

Figure 6. *In vivo* histological evaluation. (A) Hematoxylin and eosin staining of newly formed bone at week 12. (B) Masson staining of newly formed bone at week 12. The magnifications of 5×, 10×, and 20× correspond to scale bars of 500 μm, 200 μm, and 100 μm, respectively.
Notes: BD: Bone defect; HB: Host bone; IM: Implant material; NB: New bone.

potential and resorption characteristics of TCP. Previous investigations have demonstrated that *in vivo* cell-mediated BCP degradation into calcium and phosphate ions continuously supplies reconstruction substrates to defect regions, facilitating osteo-inductive bone formation.[35,36] Lu *et al.*[37] utilized 3D printing technology to precisely fabricate BCP scaffolds and, building on this, investigated the effects of varying proportions of silicon doping on the osteogenic and angiogenic capacity of BCP. Their results demonstrated that scaffolds doped with 4 mol.% silicon achieved favorable bone repair outcomes in a rabbit femoral condyle defect model. Wang *et al.*[38], based on DLP printing technology, employed the gyroid unit of a triply periodic minimal surface to design scaffolds with uniform pore sizes and pore-size gradients, exploring the balance among mechanical properties, mass transport, and biological performance in the structural design of BTE scaffolds. The present study builds upon our previous research on *in situ* surface mineralization modification technology.[29] We successfully constructed mineralized biomimetic nodules on a scaffold surface to mimic the structural and compositional features of natural bone surfaces. SEM analysis revealed heterogeneous mineralized nodules uniformly distributed across the microporous scaffold surface, confirming successful surface modification. Live/dead staining demonstrated significant cell proliferation at 72 h compared to 24 h, with BMSCs evenly adhering to the scaffold surface and peripheral pores. These results indicated that the compositionally biomimetic MiPM scaffold provides an optimal microenvironment for BMSC adhesion and proliferation. Furthermore, the ability of the scaffold to recruit osteogenic cells during bone-defect repair was validated using scratch assays and Transwell migration experiments. Both assays confirmed that the MiPM scaffold demonstrated enhanced BMSC migration, which is critical for accelerating osteogenesis in critical-sized defects. Current studies have validated that composite scaffolds fabricated with optimized nHA/β-TCP ratios significantly

enhance stem cell osteogenic differentiation and neo-osteogenesis.[39-41] Specifically, controlled dissolution of BCP ceramics elevates extracellular calcium (Ca^{2+}) and phosphate ($PO4^{3-}$) ion concentrations, thereby promoting cellular adhesion, proliferation, and ECM deposition while modulating the ionic microenvironment to favor osseous regeneration. Our experimental findings using ALP staining and ARS assays demonstrated temporally upregulated ALP expression and enhanced calcium nodule formation in BMSCs cultured on compositionally biomimetic MiPM scaffolds.

Regarding the structural design, BTE scaffolds are also termed "artificial ECM" by researchers. The core challenge lies in maximizing the retention of the osteogenic ECM microenvironment through the scaffold design.[42] Unlike the cylindrical structural designs commonly adopted in most current bone defect repair studies, which are often constrained by the critical issue of matching material degradation kinetics with the rate of nascent bone formation, we employed spherical structural scaffolds that form point-to-point contacts within the defect area. Specifically, our hollow spherical scaffold design eliminates the reliance on material degradation to free up osteogenic space; instead, it pre-reserves ample internal osteogenic cavities for the migration, proliferation, and matrix deposition of osteogenic cells. This unique structural advantage enables the scaffold to dynamically adapt to the pace of new bone tissue formation, thereby achieving efficient and coordinated bone integration with the rate of osteogenesis. This configuration preserves sufficient space for interactions between the tissue fluid and scaffold, maintains the maximum surface-area-to-volume ratio of the material, and optimizes the ECM environmental conditions from a material design perspective. The hollow structural design liberates the internal osteogenic space to match the rate of nascent bone formation. In contrast, the internal cavity enables the 3D delivery of seed cells. This structural design scheme was granted a National Utility Model Patent (Patent No.: ZL202122966951.2). SEM analysis revealed that the MiPM scaffold exhibited an intact architecture with well-defined pore morphology, surface roughness resembling that of natural bone tissue, and micropores (1–5 μm) distributed across the surface. Previous studies have indicated that microporous structures (<10 μm) enhance the scaffold surface area and roughness, improving cell adhesion and osseointegration capacity.[43] Regarding its mechanical properties, cortical bone typically exhibits an elastic modulus of 7–30 GPa[2] and a compressive strength of 100–200 MPa.[44] In contrast, trabecular bone exhibits an elastic modulus of 1–3 GPa[45] and a compressive strength of 2–20 MPa.[44] The MiPM scaffold and its composite counterpart were designed with an elastic modulus comparable to that of human cortical bone and a compressive strength intermediate between those of the cortical and trabecular bones,[46] providing sufficient mechanical support for bone defect regions. Finally, live/dead cell staining assays demonstrated that BMSCs adhering to the scaffold surface maintained robust proliferative activity, with almost no dead cells detected in the field of view, confirming that the hollow spherical structure did not cause significant impairment to cellular viability. Current studies have extensively explored structural design innovations in BTE. For example, Feng *et al.*[47] fabricated conch-like bioceramic BTE scaffolds using DLP-based 3D printing. In these scaffolds, the spiral architecture induced directional cell migration from the scaffold base to the apex, guiding oriented bone growth. Research on hollow-pillar-structured scaffolds has highlighted their capacity to provide vascularization space, enhance ion release from scaffold components, and improve the delivery of growth factors and stem cells. Notably, increased vascularized bone tissue was observed near the cortical bone interface in these designs.[8]

Regarding the bioactivity of BTE scaffolds, BMSCs often serve as one of the three essential components of BTE, accompanying the scaffold into bone defect areas to secrete endogenous repair factors and differentiate into osteoblast-like cells, thereby accelerating the bone defect repair process.[48] Previous studies have indicated that traditional 2D cell delivery models lack sufficient growth space, are prone to triggering intercellular contact inhibition, and diverge significantly from the true physiological environment *in vivo*, making it difficult to simulate key organ functional characteristics.[17,18] In contrast, 3D cell delivery models allow cells to grow in all directions, closely mimicking *in vivo* growth patterns and better preserving the structural and compositional foundations of the cellular microenvironment. Researchers have noted that the 3D culture of stem cells enhances ECM secretion and increases adhesion molecules, thereby improving the regulation of stem cell proliferation and differentiation.[49] In contrast, gelatin, a critical component of the ECM, was modified with methacryloyl groups to create GelMA, which exhibits photo-crosslinking properties and has been extensively validated for its excellent biocompatibility.[50] In this study, we fabricated a photocrosslinkable GelMA hydrogel as a 3D cell delivery carrier. Successful grafting of the methacryloyl groups onto the gelatin side chains was confirmed using FTIR and NMR analyses, and SEM further demonstrated the highly porous 3D network structure of the hydrogel. Live/Dead and cytoskeletal staining revealed enhanced BMSC proliferation and spatial distribution within the GelMA-constructed microenvironment. ALP and ARS staining,

along with quantitative analysis, showed that BMSCs in the GelMA-constructed microenvironment exhibited increased ALP expression and calcium nodule formation, indicating superior osteogenic differentiation. These results indirectly confirm the outstanding biocompatibility, high water content, and excellent permeability of the GelMA hydrogel, which collectively provide an optimal microenvironment for osteogenesis. These findings were consistent with those of previous literature.[51] RT-qPCR analysis of the expression of the osteogenesis-related genes *COL1A1* (encoding collagen type I), *BGLAP* (encoding osteocalcin), and *SPP1* (encoding osteopontin) at 7 days revealed that the 3D BMSC culture system based on GelMA significantly enhanced osteogenic gene expression compared with traditional methods. Anada *et al.*[52] designed a bone-mimetic scaffold using octacalcium phosphate and employed a GelMA hydrogel to achieve a 3D culture of BTE-critical seed cells, which were injected into the hollow medullary cavity of the scaffold, demonstrating robust bone repair outcomes. Similarly, Li *et al.*[53] developed a photocrosslinked biomimetic GelMA hydrogel scaffold that mimicked the physical and chemical structures of the natural bone ECM. They successfully repaired segmental bone defects in rats by encapsulating BMSCs within the hydrogel to reconstruct an ECM-like microenvironment. Building on these advancements, this study leveraged the hollow spherical structure of the MiPM scaffold to internally load a GelMA-based 3D BMSC delivery system, further exploring the *in vivo* bone repair efficacy of the MiPM/Gel/BMSC composite scaffold.

In this study, we established a critical-sized bone defect model using rabbit femoral condyles to further investigate the efficacy of the MiPM/Gel/BMSC composite scaffold in treating bone defects. Unlike traditional femoral condyle defect models with diameters of 4–6 mm, the 8 mm defect diameter used in this study has rarely been reported in previous literature.[54,55] Radiographic observations revealed that the defect area in the blank group remained visible at 12 weeks, confirming that the critical-sized defect model was incapable of self-healing. The MiPM group demonstrated bone repair capabilities at 4, 8, and 12 weeks, consistent with prior research findings, in which the scaffold served as an osteogenic platform and facilitated new bone ingrowth within its hollow interior.[14] Notably, the MiPM/Gel group exhibited less new bone volume at 4 weeks compared with the MiPM and MiPM/Gel/BMSC groups, which may be attributed to the incomplete degradation of GelMA during the early stage, where the residual hydrogel accumulated within the hollow spherical scaffold and interfered with bone ingrowth. Micro-CT quantitative data at 12 weeks revealed no statistically significant differences in BMD, BV/TV, Tb.Sp, or Tb.Th between the MiPM and MiPM/Gel groups ($p > 0.05$), likely because of the gradual *in vivo* degradation of GelMA during the later repair phases. This trend aligns with the findings of Kelly *et al.*,[56] where the woven bone was predominantly deposited on scaffold surfaces at 4 weeks, and larger internal void volumes facilitated enhanced osteoinduction and bone ingrowth. In contrast, the MiPM/Gel/BMSC group showed extensive new bone formation within the scaffold interior at 4 weeks, with interconnected bone bridges spanning the longest diameter of the scaffold. This phenomenon is linked to the 3D delivery of BMSCs through the hollow structure, which amplifies their osteogenic potential. By 12 weeks, the MiPM/Gel/BMSC group achieved near-identical neo-bone reconstruction to the native bone tissue inside and outside the scaffold. Micro-CT quantification confirmed significant improvements in BMD and Tb.Th compared with those in the MiPM group ($p < 0.05$), underscoring the efficacy of BCP-based scaffolds combined with the GelMA hydrogel for BMSC delivery to enhance scaffold bioactivity and accelerate bone defect repair.[57] Xu *et al.*[58] developed a BCP/GelMA composite hydrogel to construct a novel bone defect scaffold that effectively promoted BMSC osteogenic differentiation *in vitro* and successfully repaired critical-sized cranial bone defects in rats. Lai *et al.*[59] highlighted that, for relatively large-volume BTE scaffolds, seed cells struggle to migrate to the central regions, leading to uneven cell distribution and reduced osteogenic capacity. To address this issue, they encapsulated BMSCs in GelMA and combined them with ceramic materials to fabricate a cell-laden composite scaffold. In the present study, histological staining revealed that, except for the blank group, the other three groups exhibited robust new bone ingrowth at 12 weeks, with neotrabecular bone formation observed within the hollow spherical scaffolds and surrounding pores. Notably, the MiPM/Gel/BMSC group achieved complete osseointegration with the host bone, demonstrating a significantly higher new bone volume than the other groups. These findings align with those of previous studies,[60,61] which emphasized that enhancing the bioactivity of BTE scaffolds can improve osteoconduction (bone ingrowth), osseointegration (scaffold-host bone anchoring), and osteoinduction (differentiation of osteoprogenitor cells). A key insight from this study is the potential of leveraging the hollow spherical structure to load diverse seed cells and bioactive factors, offering a novel design paradigm for advancing BTE technology.

This study had certain limitations. The BCP material did not completely degrade within the 12-week observation period. Consequently, further investigations into the modifications of the BCP scaffold components are warranted to accelerate its degradation rate and synchronize it with the duration of bone repair. This will

help achieve optimal repair outcomes and offer a viable clinical approach for treating critical-sized bone defects.

5. Conclusion

In this study, a hollow, spherical, mineralized BTE scaffold was fabricated using DLP printing technology, and its interior was loaded with a 3D BMSC delivery system based on the GelMA hydrogel. The composite scaffold exhibited mechanical properties comparable to native bone tissue, along with excellent biocompatibility, enhanced osteogenic differentiation and migration of BMSCs, and upregulated expression of osteogenesis-specific mRNA markers. Radiographic and histological evaluations confirmed its efficacy in repairing critical-sized bone defects, and the 3D delivery of BMSCs significantly amplified bone tissue regeneration capacity. This novel BTE composite scaffold provides a groundbreaking design concept and therapeutic strategy for the clinical treatment of critical-sized bone defects.

Acknowledgments

None.

Funding

This research was funded by the National Key Research and Development Program of China (grant number:2024YFC2418800), the National Natural Science Foundation of China (grant number: 82402814), the Beijing Natural Science Foundation-Haidian Original Innovation Joint Fund (grant numbers: L222146, L256032), the Youth Autonomous Innovation Science Foundation of Chinese PLA General Hospital (grant number: 22QNFC009), the Youth Autonomous Innovation Science Foundation of Chinese PLA General Hospital (grant number: 22QNCZ030).

Conflict of interest

The authors declare they have no competing interests.

Author contributions

Conceptualization: Jianpeng Gao, Hufei Wang, Jie Wu, Jianheng Liu

Funding acquisition: Xiao Liu, Hufei Wang, Daohong Liu, Ming Li

Investigation: Licheng Zhang, Daohong Liu, Wei Zhang, Ming Li

Writing–original draft: Xiao Liu, Zijian Li, Jiazhi Yan

Writing–review & editing: Zhengyang Chang

Ethics approval and consent to participate

Animal experiments of this study were approved by the Ethics Committee of PLA General Hospital (Approval No.: 2022-x18-51).

Consent for publication

Not applicable.

Availability of data

Data are available from the corresponding author upon reasonable request.

References

1. Zhang Y, Lin T, Meng H, *et al*. 3D gel-printed porous magnesium scaffold coated with dibasic calcium phosphate dihydrate for bone repair in vivo. *J Orthop Transl.* 2022;33:13–23.

   doi: 10.1016/j.jot.2021.11.005

2. Turnbull G, Clarke J, Picard F, *et al*. 3D bioactive composite scaffolds for bone tissue engineering. *Bioact Mater.* 2018;3(3):278-314.

   doi: 10.1016/j.bioactmat.2017.10.001

3. Wang W, Yeung KWK. Bone grafts and biomaterials substitutes for bone defect repair: A review. *Bioact Mater.* 2017;2(4):224-247.

   doi: 10.1016/j.bioactmat.2017.05.007

4. Zhu G, Zhang T, Chen M, *et al*. Bone physiological microenvironment and healing mechanism: Basis for future bone-tissue engineering scaffolds. *Bioact Mater*. 2021;6(11):4110-4140.

   doi: 10.1016/j.bioactmat.2021.03.043

5. Beigi MH, Safaie N, Nasr-Esfahani MH, Kiani A. 3D Titania Nanofiber-Like Webs Induced by Plasma Ionization: A New Direction for Bioreactivity and Osteoinductivity Enhancement of Biomaterials. *Sci Rep*. 2019;9(1):17999.

   doi: 10.1038/s41598-019-54533-z

6. Qin Y, Wen P, Guo H, *et al*. Additive manufacturing of biodegradable metals: Current research status and future perspectives. *Acta Biomater.* 2019;98:3-22.

   doi: 10.1016/j.actbio.2019.04.046

7. Valtanen RS, Yang YP, Gurtner GC, Maloney WJ, Lowenberg DW. Synthetic and bone tissue engineering graft substitutes: What is the future? *Injury*. 2021;52 Suppl 2:S72-S77.

   doi: 10.1016/j.injury.2020.07.040

8. Yin S, Zhang W, Zhang Z, Jiang X. Recent Advances in Scaffold Design and Material for Vascularized Tissue-Engineered Bone Regeneration. *Adv Healthcare Mater*. 2019;8(10):e1801433.

   doi: 10.1002/adhm.201801433

9. He F, Ye J. In vitro degradation, biocompatibility, and in

vivo osteogenesis of poly(lactic-co-glycolic acid)/calcium phosphate cement scaffold with unidirectional lamellar pore structure. *J Biomed Mater Res Part A*. 2012;100(12):3239-3250.

doi: 10.1002/jbm.a.34265

10. Wang X, Lin M, Kang Y. Engineering Porous β-Tricalcium Phosphate (β-TCP) Scaffolds with Multiple Channels to Promote Cell Migration, Proliferation, and Angiogenesis. *ACS Appl. Mater Interfaces.* 2019;11(9):9223-9232.

doi: 10.1021/acsami.8b22041

11. Freytes DO, Kang JW, Marcos-Campos I, Vunjak-Novakovic G. Macrophages modulate the viability and growth of human mesenchymal stem cells. *J Cell Biochem*. 2013;114(1):220-229.

doi: 10.1002/jcb.24357

12. Duda GN, Geissler S, Checa S, Tsitsilonis S, Petersen A, Schmidt-Bleek K. The decisive early phase of bone regeneration. *Nat Rev Rheumatol.* 2023;19(2):78-95.

doi: 10.1038/s41584-022-00887-0

13. Liu X, Gao J, Liu J, Zhang L, Li M. Inhibiting the "isolated island" effect in simulated bone defect repair using a hollow structural scaffold design. *Front Bioeng Biotechnol.* 2024;12:1362913.

doi: 10.3389/fbioe.2024.1362913

14. Liu X, Gao J, Liu J, *et al*. Three-Dimensional-Printed Spherical Hollow Structural Scaffolds for Guiding Critical-Sized Bone Regeneration. *ACS Biomater Sci Eng*. 2024;10(4):2581-2594.

doi: 10.1021/acsbiomaterials.3c01956

15. Kim HD, Amirthalingam S, Kim SL, Lee SS, Rangasamy J, Hwang NS. Biomimetic Materials and Fabrication Approaches for Bone Tissue Engineering. *Adv Healthcare Mater*. 2017;6(23).

doi: 10.1002/adhm.201700612

16. Lowe B, Ottensmeyer MP, Xu C, He Y, Ye Q, Troulis MJ. The Regenerative Applicability of Bioactive Glass and Beta-Tricalcium Phosphate in Bone Tissue Engineering: A Transformation Perspective. *J Funct Biomater*. 2019;10(1).

doi: 10.3390/jfb10010016

17. Chen CS. 3D Biomimetic Cultures: The Next Platform for Cell Biology. *Trends Cell Biol.* 2016;26(11):798-800.

doi: 10.1016/j.tcb.2016.08.008

18. Payr S, Rosado-Balmayor E, Tiefenboeck T, *et al*. Direct comparison of 3D and 2D cultivation reveals higher osteogenic capacity of elderly osteoblasts in 3D. *J Orthop Surg Res*. 2021;16(1):13.

doi: 10.1186/s13018-020-02153-z

19. Laschke MW, Menger MD. Life is 3D: Boosting Spheroid Function for Tissue Engineering. *Trends Biotechnol.* 2017;35(2):133-144.

doi: 10.1016/j.tibtech.2016.08.004

20. Bicer M, Cottrell GS, Widera D. Impact of 3D cell culture on bone regeneration potential of mesenchymal stromal cells. *Stem Cell Res Ther.* 2021;12(1):31.

doi: 10.1186/s13287-020-02094-8

21. Wang J, Wang T, Zhang F, *et al*. Roles of circular RNAs in osteogenic differentiation of bone marrow mesenchymal stem cells (Review). *Mol Med Rep*. 2022;26(1).

doi: 10.3892/mmr.2022.12743

22. Hou Y, Lin W, Li Y, *et al*. De-osteogenic-differentiated mesenchymal stem cells accelerate fracture healing by mir-92b. *J Orthop Transl.* 2021;27:25-32.

doi: 10.1016/j.jot.2020.10.009

23. Ma L, Wang X, Zhou Y, *et al*. Biomimetic Ti-6Al-4V alloy/gelatin methacrylate hybrid scaffold with enhanced osteogenic and angiogenic capabilities for large bone defect restoration. *Bioact Mater*. 2021;6(10):3437-3448.

doi: 10.1016/j.bioactmat.2021.03.010

24. Zhu J, Marchant RE. Design properties of hydrogel tissue-engineering scaffolds. *Expert Rev Med Devices*. 2011;8(5):607-26.

doi: 10.1586/erd.11.27

25. Gao C, Sow WT, Wang Y, *et al*. Hydrogel composite scaffolds with an attenuated immunogenicity component for bone tissue engineering applications. *J Mater Chem B*. 2021;9(8):2033-2041.

doi: 10.1039/d0tb02588g

26. Li J, Chen M, Fan X, Zhou H. Recent advances in bioprinting techniques: approaches, applications and future prospects. *J Transl Med*. 2016;14:271.

doi: 10.1186/s12967-016-1028-0

27. Li R, Zhou C, Chen J, *et al*. Synergistic osteogenic and angiogenic effects of KP and QK peptides incorporated with an injectable and self-healing hydrogel for efficient bone regeneration. *Bioact Mater*. 2022;18:267-283.

doi: 10.1016/j.bioactmat.2022.02.011

28. Li J, Cui X, Lindberg GCJ, *et al*. Hybrid fabrication of photo-clickable vascular hydrogels with additive manufactured titanium implants for enhanced osseointegration and vascularized bone formation. *Biofabrication*. 2022;14(3).

doi: 10.1088/1758-5090/ac6051

29. Liu X, Gao J, Cui X, *et al*. Functionalized 3D-Printed PLA Biomimetic Scaffold for Repairing Critical-Size Bone Defects. *Bioengineering*. 2023;10(9).

doi: 10.3390/bioengineering10091019

30. Kokubo T, Takadama H. How useful is SBF in predicting in

vivo bone bioactivity? *Biomaterials*. 2006;27(15):2907-2915.

doi: 10.1016/j.biomaterials.2006.01.017

31. Heise T, Sawyer AY, Hirai T, Schaible S, Sy H, Wickramasekara S. Report on investigation of ISO 10993-12 extraction conditions. *Regul Toxicol Pharmacol RTP*. 2022;131:105164.

doi: 10.1016/j.yrtph.2022.105164

32. Zhang Y, Xu Y, Kong H, *et al*. Microneedle system for tissue engineering and regenerative medicine. *Exploration*. 2023;3(1):20210170.

doi: 10.1002/exp.20210170

33. Fan Y, Zheng L, Jin M, Li X, Li ZA, Wang X. Mussel-mimetic polysaccharide-based injectable hydrogels for biomedical applications. *BMEMat*. 2024;2(4):e12089.

doi: 10.1002/bmm2.12089

34. Miller MI, Brightman AO, Epstein FH, *et al*. BME 2.0: Engineering the Future of Medicine. *BME Front*. 2023;4:0001.

doi: 10.34133/bmef.0001

35. LeGeros RZ. Properties of osteoconductive biomaterials: calcium phosphates. *Clin Orthop Relat Res*. 2002;(395):81-98.

doi: 10.1097/00003086-200202000-00009

36. Ko CL, Chen WC, Chen JC, *et al*. Properties of osteoconductive biomaterials: calcium phosphate cement with different ratios of platelet-rich plasma as identifiers. *Mater Sci Eng C Mater Biol Appl*. 2013;33(6):3537-3544.

doi: 10.1016/j.msec.2013.04.042

37. Lu T, Li G, Zhang L, Yuan X, Wu T, Ye J. Optimizing silicon doping levels for enhanced osteogenic and angiogenic properties of 3D-printed biphasic calcium phosphate scaffolds: An in vitro screening and in vivo validation study. *Mater Today Bio*. 2024;28:101203.

doi: 10.1016/j.mtbio.2024.101203

38. Wang Y, Liu Y, Chen S, *et al*. Enhancing bone regeneration through 3D printed biphasic calcium phosphate scaffolds featuring graded pore sizes. *Bioact Mater*. 2025;46:21-36.

doi: 10.1016/j.bioactmat.2024.11.024

39. Touri M, Moztarzadeh F, Osman NAA, Dehghan MM, Mozafari M. 3D-printed biphasic calcium phosphate scaffolds coated with an oxygen generating system for enhancing engineered tissue survival. *Mater Sci Eng C Mater Biol Appl*. 2018;84:236-242.

doi: 10.1016/j.msec.2017.11.037

40. Bajpai I, Kim DY, Kyong-Jin J, Song IH, Kim S. Response of human bone marrow-derived MSCs on triphasic Ca-P substrate with various HA/TCP ratio. *J Biomed Mater Res Part B Appl Biomater*. 2017;105(1):72-80.

doi: 10.1002/jbm.b.33538

41. Ng AM, Tan KK, Phang MY, *et al*. Differential osteogenic activity of osteoprogenitor cells on HA and TCP/HA scaffold of tissue engineered bone. *J Biomed Mater Res Part A*. 2008;85(2):301-12.

doi: 10.1002/jbm.a.31324

42. Xue J, Qin C, Wu C. 3D printing of cell-delivery scaffolds for tissue regeneration. *Regen Biomater*. 2023;10:rbad032.

doi: 10.1093/rb/rbad032

43. Bose S, Sarkar N. Natural Medicinal Compounds in Bone Tissue Engineering. *Trends Biotechnol*. 2020;38(4):404-417.

doi: 10.1016/j.tibtech.2019.11.005

44. Lefèvre E, Farlay D, Bala Y, *et al*. Compositional and mechanical properties of growing cortical bone tissue: a study of the human fibula. *Sci Rep*. 2019;9(1):17629.

doi: 10.1038/s41598-019-54016-1

45. Qin Y, Liu A, Guo H, *et al*. Additive manufacturing of Zn-Mg alloy porous scaffolds with enhanced osseointegration: In vitro and in vivo studies. *Acta Biomater*. 2022;145:403-415.

doi: 10.1016/j.actbio.2022.03.055

46. Qu X, Cui W, Yang F, *et al*. The effect of oxygen plasma pretreatment and incubation in modified simulated body fluids on the formation of bone-like apatite on poly(lactide-co-glycolide) (70/30). *Biomaterials*. 2007;28(1):9-18.

doi: 10.1016/j.biomaterials.2006.08.024

47. Feng B, Zhang M, Qin C, *et al*. 3D printing of conch-like scaffolds for guiding cell migration and directional bone growth. *Bioact Mater*. 2023;22:127-140.

doi: 10.1016/j.bioactmat.2022.09.014

48. Futrega K, Mosaad E, Chambers K, Lott WB, Clements J, Doran MR. Bone marrow-derived stem/stromal cells (BMSC) 3D microtissues cultured in BMP-2 supplemented osteogenic induction medium are prone to adipogenesis. *Cell Tissue Res*. 2018;374(3):541-553.

doi: 10.1007/s00441-018-2894-y

49. Potapova IA, Gaudette GR, Brink PR, *et al*. Mesenchymal stem cells support migration, extracellular matrix invasion, proliferation, and survival of endothelial cells in vitro. *Stem Cells*. 2007;25(7):1761-1768.

doi: 10.1634/stemcells.2007-0022

50. Yue K, Trujillo-de Santiago G, Alvarez MM, Tamayol A, Annabi N, Khademhosseini A. Synthesis, properties, and biomedical applications of gelatin methacryloyl (GelMA) hydrogels. *Biomaterials*. 2015;73:254-271.

doi: 10.1016/j.biomaterials.2015.08.045

51. Gungor-Ozkerim PS, Inci I, Zhang YS, Khademhosseini A, Dokmeci MR. Bioinks for 3D bioprinting: an overview. *Biomater Sci*. 2018;6(5):915-946.

doi: 10.1039/c7bm00765e

52. Anada T, Pan CC, Stahl AM, *et al*. Vascularized Bone-Mimetic Hydrogel Constructs by 3D Bioprinting to Promote Osteogenesis and Angiogenesis. *Int J Mol Sci*. 2019;20(5):1096.

doi: 10.3390/ijms20051096

53. Li J, Wang W, Li M, *et al*. Biomimetic Methacrylated Gelatin Hydrogel Loaded With Bone Marrow Mesenchymal Stem Cells for Bone Tissue Regeneration. *Front Bioeng Biotechnol*. 2021;9:770049.

doi: 10.3389/fbioe.2021.770049

54. Guo C, Qi J, Liu J, *et al*. The Ability of Biodegradable Thermosensitive Hydrogel Composite Calcium-Silicon-Based Bioactive Bone Cement in Promoting Osteogenesis and Repairing Rabbit Distal Femoral Defects. *Polymers*. 2022;14(18).

doi: 10.3390/polym14183852

55. Zhang Y, Cui X, Zhao S, *et al*. Evaluation of injectable strontium-containing borate bioactive glass cement with enhanced osteogenic capacity in a critical-sized rabbit femoral condyle defect model. *ACS Appl Mater Interfaces*. 2015;7(4):2393-2403.

doi: 10.1021/am507008z

56. Kelly CN, Wang T, Crowley J, *et al*. High-strength, porous additively manufactured implants with optimized mechanical osseointegration. *Biomaterials*. 2021;279:121206.

doi: 10.1016/j.biomaterials.2021.121206

57. Zhi W, Wang X, Sun D, *et al*. Optimal regenerative repair of large segmental bone defect in a goat model with osteoinductive calcium phosphate bioceramic implants. *Bioact Mater*. 2022;11:240-253.

doi: 10.1016/j.bioactmat.2021.09.024

58. Xu R-J, Ma J-J, Xiao Y, *et al*. A biphasic calcium phosphate/acylated methacrylate gelatin composite hydrogel promotes osteogenesis and bone repair. *Connect Tissue Res*. 2023;64(5):445-456.

doi: 10.1080/03008207.2023.2212067

59. Lai J, Wang C, Liu J, *et al*. Low temperature hybrid 3D printing of hierarchically porous bone tissue engineering scaffolds within situ delivery of osteogenic peptide and mesenchymal stem cells. *Biofabrication*. 2022;14(4).

doi: 10.1088/1758-5090/ac84b0

60. Kim SS, Sun Park M, Jeon O, Yong Choi C, Kim BS. Poly(lactide-co-glycolide)/hydroxyapatite composite scaffolds for bone tissue engineering. *Biomaterials*. 2006;27(8):1399-1409.

doi: 10.1016/j.biomaterials.2005.08.016

61. Albrektsson T, Johansson C. Osteoinduction, osteoconduction and osseointegration. *Eur Spine J*. 2001;10(Suppl 2):S96-S101.

doi: 10.1007/s005860100282